Journal of
Applied Crystallography
ISSN 0021-8898

Received 7 March 2008
Accepted 1 October 2008

Microstrain and grain-size analysis from diffraction peak width and graphical derivation of high-pressure thermomechanics

Yusheng Zhao* and Jianzhong Zhang

LANSCE Division, Los Alamos National Laboratory, Los Alamos, NM 87545, USA. Correspondence e-mail: yzhao@lanl.gov

An analytical method is presented for deriving the thermomechanical properties of polycrystalline materials under high-pressure (P) and high-temperature (T) conditions. This method deals with non-uniform stress among heterogeneous crystal grains and surface strain in nanocrystalline materials by examining peak-width variation under different P–T conditions. Because the method deals directly with lattice d spacing and local deformation caused by stress, it can be applied to process any diffraction profile, independent of detection mode. In addition, a correction routine is developed using diffraction elastic ratios to deal with severe surface strain and/or strain anisotropy effects related to nano-scale grain sizes, so that significant data scatter can be reduced in a physically meaningful way. Graphical illustration of the resultant microstrain analysis can identify micro/local yields at the grain-to-grain interactions resulting from high stress concentration, and macro/bulk yield of the plastic deformation over the entire sample. This simple and straightforward approach is capable of revealing the corresponding micro and/or macro yield stresses, grain crushing or growth, work hardening or softening, and thermal relaxation under high-P–T conditions, as well as the intrinsic residual strain and/or surface strain in the polycrystalline bulk. In addition, this approach allows the instrumental contribution to be illustrated and subtracted in a straightforward manner, thus avoiding the potential complexities and errors resulting from instrument correction. Applications of the method are demonstrated by studies of α-SiC (6H, moissanite) and of micro- and nanocrystalline nickel by synchrotron X-ray and time-of-flight neutron diffraction.

1. Diffraction analysis of crystalline deformation

Stress–strain measurement to derive yield strength is a conventional practice for engineering materials. Recent advancements in diffraction techniques with high-intensity synchrotron X-ray and time-of-flight neutron radiation allow deformation studies for bulk samples at the atomic level (Weidner *et al.*, 1994; Zhao *et al.*, 1994, 2007; Zhang *et al.*, 2002; Brown *et al.*, 2003; Chen *et al.*, 2005; Qian *et al.*, 2005; Zhao & Zhang, 2007; Wang *et al.*, 2007). By applying a stress field to a crystalline sample and monitoring the shift of the diffraction peak positions in a compressive test, one can derive the overall strain data (macrostrain) and thus the constitutive equations of the sample materials. The crystal lattice responds elastically to the applied stress field before the plastic yield, and significant stress heterogeneity occurs within the polycrystalline sample. The local stress varies from grain to grain, owing to different crystalline orientations relative to the loading direction, and also because of stress concentration at grain contacts during powder compaction. Correspondingly, the local strain (microstrain) at the contact points between crystal grains can span a very wide range and, as a result, the diffraction peaks broaden significantly. Detailed peak-width analysis can reveal micro/local yields at the high stress concentration portion of the grain contacts. At this stage, the bulk sample still performs within the elastic regime with significant nonlinear components. Consistent with the classical definition, the microstrains determined in this work before the bulk yield are elastic, whereas deviation from the linear variation of microstrain marks the onset of plastic deformation, in the sense that the bulk material can no longer support further differential or shear stress in an elastic sense. Correspondingly, the diffraction peak widths after the bulk yield would either remain at a constant level or broaden or sharpen to a certain extent, depending on the yield strength of the material as a function of high-P–T conditions. In this article, we deal only with microscopic strain and stress derived from diffraction peak-width changes during loading, unloading and heating.

The diffraction profile is a convolution function of instrument response, grain-size distribution and crystal lattice deformations along the diffraction vector. In high-tempera-

ture annealing experiments at atmospheric pressure, the diffraction peak width narrows with increasing temperature, reflecting the relaxation of residual strain or, in the case of nanocrystalline materials, demonstrating both the surface strain relaxation and grain growth. During a high-pressure compression experiment, the widths of the diffraction peaks broaden and approach the maximum as (i) the grain-size reduction through the crushing process reaches its minimum; and (ii) the deviatoric stress approaches the ultimate yield stress and the sample material deforms in the manner of plastic flow. All diffraction techniques observe the d spacing and intensity of various crystallographic planes with Miller indices hkl to derive the atomic settings of the crystal lattice, regardless of the detection mode (energy dispersive, angular dispersive and/or time-of-flight). We can thus plot the diffraction peak profile in terms of the lattice d spacing (in ångströms), which is a universal length scale that is independent of the detection mode.

We conducted a high-P–T experiment on moissanite (6H-SiC) using energy-dispersive synchrotron X-ray diffraction and a Kawai-type T-Cup high-pressure system (Vaughan *et al.*, 1998). T-Cup is a 6–8 double-stage multi-anvil high-pressure module, with a truncation edge length of 2 mm on eight tungsten carbide cubes and a capability of generating high pressures up to 20 GPa. The powder moissanite sample was packed into a cylindrical boron epoxy sample chamber of 1 mm diameter and 1 mm length, which was then loaded into an octahedral boron epoxy pressure medium of 8 mm edge-length. Two rhenium strips were placed on the top and bottom of the sample to provide resistive heating. The loading conditions and diffraction geometry for the multi-anvil presses used in this study have been described previously (Weidner *et al.*, 1994; Chen *et al.*, 2005). Briefly, the incident X-ray beam for diffraction is perpendicular to both the loading direction and the maximum stress vector σ_1 (*i.e.* the vertical axis in the laboratory coordinate system). Assuming cylindrical symmetry of the stress field in our multi-anvil cell, we have $\sigma_1 \neq \sigma_2 = \sigma_3$ (where σ_2 or σ_3 is the minimum stress vector), indicating that, on top of a hydrostatic stress field, our loading system generates a statistically uniform differential stress throughout the sample. Although the loading force from the hydraulic ram is uniaxial, the simultaneous movement of the first-stage anvils toward the center of an octahedral or cubic high-pressure cell would result in triaxial compression of the sample. The moissanite powders were first compressed to 18.6 GPa at room temperature using a hydraulic ram and then heated to a maximum temperature of 1473 K. Along this P–T path, X-ray diffraction data were collected at selected pressures and temperatures. Both the peak position (d spacing) and the full width at half-maximum (FWHM) were determined using a Gaussian fit of the diffracted intensity. For all high-pressure data reported in this paper, the pressures were determined using the Decker (1971) scale for NaCl.

A number of diffraction profiles at ambient, high-P and high-P–T conditions are plotted in Fig. 1 for moissanite to show peak-width changes. The broadening and narrowing of the diffraction peaks indicate the increase and decrease of the stress level applied to the crystalline grains. During the compression portion of the cycle, the diffraction lines broaden asymmetrically before the macro/bulk yield, with the larger-d-spacing side of the peak remaining unchanged (black and green patterns in Fig. 1, insert). This unsymmetrical broadening suggests that quite a large proportion of the grains do not experience much stress and only a certain proportion of the grains support the applied loading force, which is a typical phenomenon for hard materials during high-P compaction (Weidner *et al.*, 1994; Qian *et al.*, 2005). After the macro/bulk yield, however, both sides of the diffraction peaks move to smaller d-spacing values (dark-blue and purple patterns in Fig. 1, insert). The diffraction peaks become sharpened in the high-P–T plastic flow stages.

The diffraction profile can be expressed in Gaussian form in terms of the lattice d spacing (Å), giving a universal expression that is independent of the detection mode:

$$\mathrm{Int}(d) \propto \exp\left\{-\left[(d - d_{hkl})/s\right]^2\right\}, \qquad (1)$$

where $\mathrm{Int}(d)$ denotes the diffraction peak intensity as a function of d spacing and s is a statistical scale parameter to define the diffraction peak width, which is correlated to the often-used FWHM by $\mathrm{FWHM} = 2s(\ln 2)^{1/2}$. The s in equation (1) is more conventionally defined as the standard deviation σ for a Gaussian distribution, and the relationship between FWHM and σ is $\mathrm{FWHM} = 2(2\ln 2)^{1/2}\sigma$. In this study, we

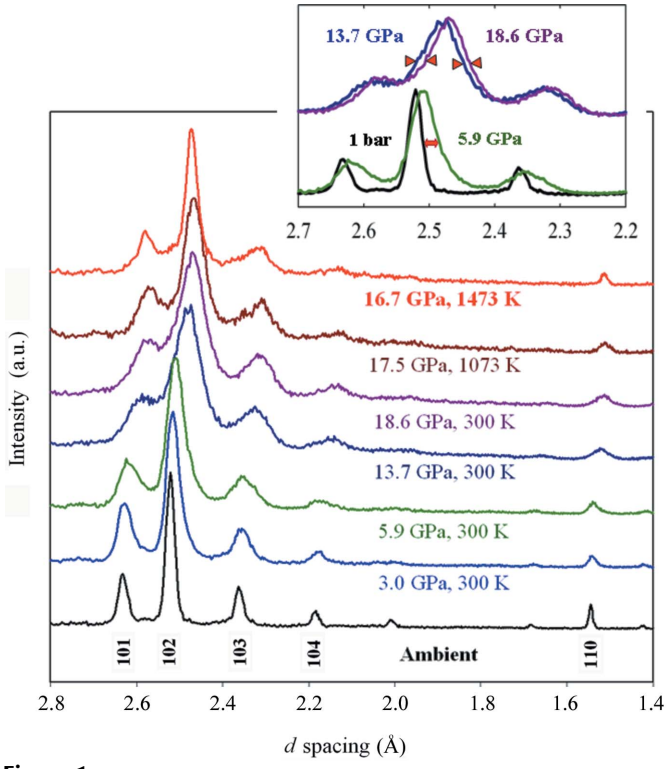

Figure 1
The diffraction patterns of moissanite (α-6H-SiC) under selected pressure and temperature conditions. The peak intensities of the hkl diffractions at high P–T are normalized relative to that of (102) under ambient conditions for width-comparison purposes. The insert shows an enlargement of the (101), (102) and (103) diffraction lines.

denote the observed FWHM as $\Delta d_{\rm obs} = (d^2 - \overline{d}^2)^{1/2} = \Delta d$(FWHM), reflecting the lattice d-spacing span around the mean $\overline{d}$ of a particular diffraction peak (for simplicity, we use d to denote $\overline{d}$ throughout this paper). The profiles of the observed diffraction peaks are the results of convoluted functions with multiple effects of instrument response, grain size and microstrain (lattice deformation) as a result of stress heterogeneity and dislocation density at high P–T. Thereafter, the integrated width of the diffraction peak can be deconvoluted through Fourier transformation, *i.e.*

$$\Delta d_{\rm obs}^2 = \Delta d_{\rm ins}^2 + \Delta d_{\rm size}^2 + \Delta d_{\varepsilon}^2. \quad (2)$$

Here, Δd_{ε} and $\Delta d_{\rm size}$ are, respectively, the microstrain and grain size contributions to the observed peak width $\Delta d_{\rm obs}$(FWHM) under any P–T conditions, and $\Delta d_{\rm ins}$ is the peak width at a stress-free state, usually referring to the instrument contribution. The strain, $\varepsilon = \Delta d/d$, directly reveals the deformation of the crystal lattice from $\overline{d}_{hkl} + \delta d$ to $\overline{d}_{hkl} - \delta d$ for the specific d_{hkl} plane at a certain stress level. For the high-P–T diffraction experiment, both macrostrain (deviatoric shift of the diffraction lines, also referred to as the uniform strain) and microstrain (as manifested by the broadening of the diffraction peaks, also referred to as the non-uniform strain) effects can superimpose upon the hydrostatic pressure compression, in addition to the P–V–T equation-of-state (EOS) response of the crystal lattice. The diffraction peak widths reach a maximum as the deviatoric stress approaches the ultimate yield stress or as the micro/local yields eventually develop into a macro/bulk yield. Plastic or viscous flow occurs when the deviatoric component (relative to the hydrostatic component) exceeds the high-P–T yield strength, $\Delta\sigma \geq \sigma_{\rm y}$, which is actually a simplified Von Mises (octahedral shear stress) criterion. Strictly speaking, equation (2) is only true if all of the convoluted functions are Gaussian. As a result, the diffraction profile analyses throughout this work were based on a simplification of a Gaussian expression for a diffraction peak. The non-Gaussian components typically exist because of complicated contributions to a peak profile, which could introduce errors in the peak-width determination. However, the standard deviations of the peak-width determination based on a Gaussian fit are generally within 5% for all examples presented in this work. In addition, some errors associated with the non-Gaussian contributions would be smeared out owing to the relative nature of the graphical approach (subtraction) for the stress determination, as discussed below.

We consider the straightforward strain expression $\varepsilon = \Delta d/d$, and thus derive the microstrain using the universal length scale of the d spacing. By rewriting equation (2), we obtain

$$\left\{\Delta d_{\rm obs}^2 - \Delta d_{\rm ins}^2\right\} = \Delta d_{\rm size}^2 + \varepsilon^2 d^2, \quad (3)$$

where d is the d spacing of an hkl lattice plane at any P–T conditions. Equation (3) is a typical $y = a + bx$ plot, a being the ordinate intercept and b the plot slope. This approach modifies the Williamson–Hall (Williamson & Hall, 1953) plot (referred to as WH, see also discussion below) to cover all diffraction detection modes. Supposedly, the ordinate intercepts $\Delta d_{\rm size}^2$ of the $\{\Delta d_{\rm obs}^2 - \Delta d_{\rm ins}^2\}$ *versus* $d^2(P, T)$ plot for a number of hkl diffraction indices should provide information on the average grain size L. However, this interception usually presents a rather large error and does not work well for grains larger than micrometre size. Also, in some cases (see later discussion), it becomes negative and is therefore physically meaningless. Nevertheless, the microstrain can be derived from the slope ε^2 of the $\{\Delta d_{\rm obs}^2 - \Delta d_{\rm ins}^2\}$ *versus* $d^2(P, T)$ plot, or, in a more straightforward way, it can also be readily derived from the slope ε of the simplified $(\Delta d_{\rm obs}^2 - \Delta d_{\rm ins}^2)^{1/2}$ *versus* $d(P, T)$ plot for a number of hkl diffraction indices, *i.e.*

$$\varepsilon = \Delta d_{\varepsilon}/d = (\Delta d_{\rm obs}^2 - \Delta d_{\rm ins}^2)^{1/2}/d(P, T). \quad (4)$$

The microstrain ε thus derived neglects the effect of grain size and subtracts the instrumental contribution observed under ambient stress-free conditions, *i.e.* $\varepsilon = 0$ at $P = 0$ (we will discuss the residual strain situation further below). Therefore, the determined strain is the 'applied strain', represented as the ratio of peak width to peak position, $\varepsilon = \Delta d/d$. The microstrain is the dominant factor for peak-width broadening in microcrystalline materials under severe deviatoric stress conditions in high-pressure experiments.

Equation (4) is applied to re-analyze the high-P–T energy-dispersive X-ray diffraction data on microcrystalline moissanite (α-6H SiC) (Zhang *et al.*, 2002), as plotted in Fig. 1. During the compression portion of the loading cycle, the diffraction lines broaden asymmetrically up to 11.8 GPa, with the larger d-spacing side of the peak remaining unchanged. The obvious tails on the small d-spacing sides suggest that quite a large proportion of the grains do not experience much stress and only a certain proportion of the grains have been deformed. After moissanite yields at higher pressures (P = 13.7–18.6 GPa), both sides of the diffraction peaks move to smaller d-spacing values (Fig. 1, insert), indicating homogeneous compression over all of the moissanite grains. The diffraction peaks become symmetric as well as narrowed in the plastic flow stage, as shown by the data collected during the high-P–T heating cycle. We plot six sets of hkl data in Fig. 2 to illustrate the strain (slope) changes associated with P–T variations, with the data corresponding to the Fig. 1 diffraction profiles. Increasing pressure also makes the strain data gradually scattered, but they can still be fitted to straight lines very well. The microstrains of moissanite under different P–T conditions are thus derived from the slopes of the linear plots.

The deviatoric stresses are derived through a stress–strain relationship of $\sigma = E\varepsilon$, where E is Young's modulus. We applied an aggregate Young's modulus, E = 447 GPa, for moissanite (Feng *et al.*, 1996) with the bulk modulus equal to 220 GPa and the shear modulus to 193 GPa, and the derived stresses under all experimental conditions are plotted as a function of pressure and temperature in Fig. 3 to show the high-P–T yield process of moissanite. In the present triaxial high-pressure compression experiments, the diffraction optics detect the deformation of the lattice planes under the maximum loading stress (σ_1). The yield stress thus derived is the maximum deviatoric stress that the crystalline moissanite sample can support under the given high-P–T conditions.

From the Fig. 3 plots, one can clearly identify a bend (kink) near 3.0 GPa in the elastic stage, as well as plastic yield of the moissanite sample around 12.0 GPa under high-pressure loading. We consider that the bending at P = 3.0 GPa represents a micro/local yield, *i.e.* plastic deformation at grain-to-grain contacts because of the high stress concentration. The yield point that represents macro/bulk plastic deformation of the entire sample can be derived from the intersection of the elastic loading stage in the range 3.0–12.0 GPa and the ductile flowing stage at $P > 12$ GPa. The onset pressure for the yield is P = 12 GPa and the corresponding high-P yield stress is derived as $\sigma_y \simeq 13.5$ GPa (Fig. 3, left). In the pressure range 12.0–18.6 GPa, the yield stress maintains a nearly constant value with minor work softening. As the temperature increases to above T = 700 K, the yield stress of moissanite decreases at a rate of $d\sigma_y/dT = -1.34 \times 10^{-2}$ GPa K^{-1} for the temperature range 700 < T < 1500 K (Fig. 3, right). The thermally induced relaxation rates of the yield stress should be a function of pressure, and we expect the $d\sigma_y/dT$ rate to have a much higher absolute value under atmospheric pressure conditions. There are still applied stresses in the moissanite sample at the highest temperature of 1500 K, indicating its superb high-T strength. Further heating to higher temperatures (at $T > 2000$ K, as projected by the strength reduction slope) is needed to have total relaxation of the applied stress, where the instrument baseline to the initial residual stress states under ambient conditions may be reached.

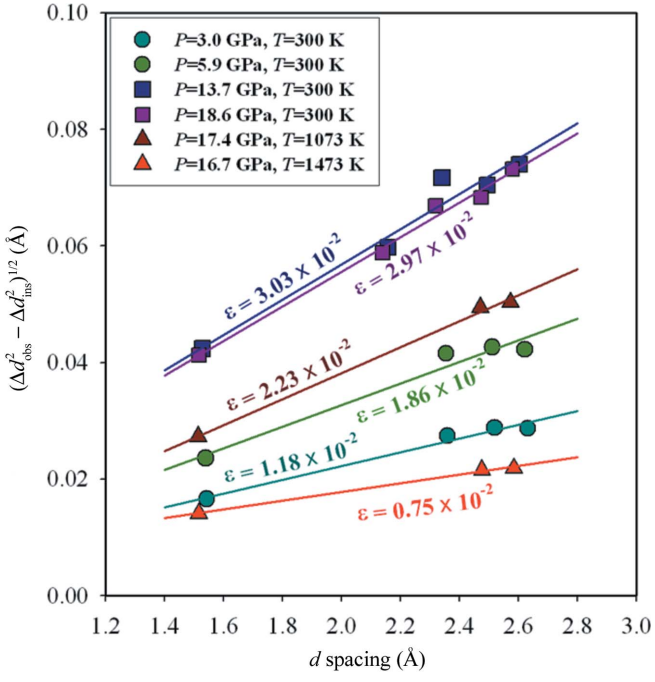

Figure 2
A plot of $(\Delta d^2_{obs} - \Delta d^2_{ins})^{1/2}$ *versus* $d(P, T)$ for moissanite, according to equation (4). The straight lines show the linear regression results and the slopes provide microstrain information at the various indicated P–T. Each of the six data sets plotted here was obtained from the corresponding diffraction profile shown in Fig. 1. The errors in $(\Delta d^2_{obs} - \Delta d^2_{ins})^{1/2}$ are smaller than or comparable to the size of the plotted symbols.

α-SiC (6H) has previously been studied under shock conditions (Feng *et al.*, 1998). At a stress approximately twice the Hugoniot elastic limit (23 GPa), the maximum shear stress (τ) that can be supported by moissanite was found to be 7.0 GPa. This is equivalent to a differential stress of 14.0 GPa based on Hook's relation $\sigma = 2\tau$, which is in good agreement with the yield stress of 13.5 GPa derived using equation (4) in this study. A similarly excellent match of the differential stress (derived from the peak broadening) and the doubled shear stress (derived from pure-shear spontaneous strain) can also be found in the high-P–T diffraction study by Zhao *et al.* (1994).

2. Cyclic loading loop and energy dissipation

We apply a comparative approach for microstrain analysis between sample pairs to illustrate the differences between nanocrystalline and microcrystalline Ni (referred to hereinafter as nano-Ni and micron-Ni, respectively) at room temperature. The micron-Ni powders were obtained commercially and were 99.8% pure with a grain-size distribution of 3–7 µm. The nano-Ni powders used in this study were prepared by ball-milling, starting from coarse-grained powders of Ni (< 840 µm, 99.999%). The powder (5 g) was ball-milled for 30 h using a SPEX 8000 mill, hardened-steel vials and 30 1 g hardened steel balls. The SPEX mill was operated inside an argon-filled glove box containing less than 1 p.p.m. oxygen. Based on peak-width analysis of X-ray diffraction under ambient conditions, the nano-Ni powders have an average grain size of 12–13 nm. Synchrotron X-ray diffraction experiments were conducted using a mixture of amorphous boron and epoxy resin as the pressure-transmitting medium. The nano-Ni and micron-Ni powders were studied at room temperature in both loading and unloading cycles using a DIA-type cubic anvil apparatus (Weidner *et al.*, 1992). The two samples were symmetrically loaded into a

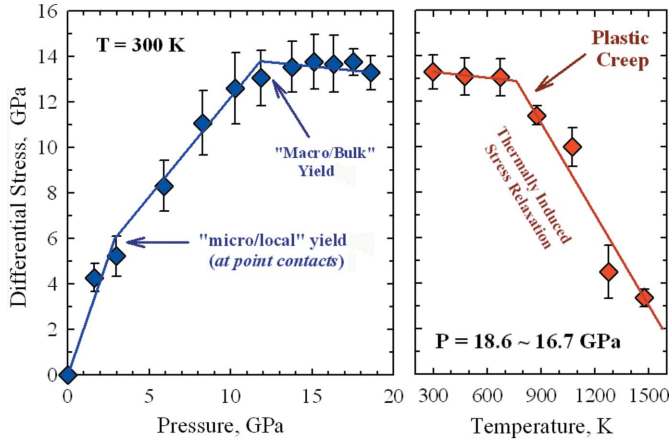

Figure 3
Applied stresses for moissanite as functions of pressure and temperature. The errors plotted here are those of the least-squares fit of the data in Fig. 2 (multiplied by Young's modulus); the uncertainties in $(\Delta d^2_{obs} - \Delta d^2_{ins})^{1/2}$ were not included for error estimation. The lines drawn here are a guide to the eye and are not the result of a model fit. See text for detailed discussion.

cylindrical boron nitride (BN) capsule, separated by a layer of NaCl; they thus experience identical P–T conditions. We have determined the applied strains from two separate measurements to maximum pressures of 1.4 and 6.0 GPa, and with much smaller pressure step intervals, because nickel (metal) is much softer than moissanite (hard ceramic). Our results show that the absolute values of the applied strain for nano-Ni at the maximum pressure are three to four times higher than those for micron-Ni. To make comparisons easier, we normalize the observed strain relative to the maximum strain at the highest pressure:

$$\varepsilon_{hkl}^{\rm norm} = (\Delta d/d)_{hkl}/(\Delta d/d)_{hkl}^{\max P}. \quad (5)$$

Our analysis shows that the individual lattice planes have different strains upon loading (Zhao *et al.*, 2007) for both nano-Ni and micron-Ni, and this behavior will be discussed in more detail in a later section of this paper. Plotted in Fig. 4 are the average values of four different lattice planes of the two experiments, $P_{\rm max}$ = 1.4 GPa (left) and $P_{\rm max}$ = 6.0 GPa (right), using the strain normalization approach [equation (5)]. It is important to note that, although the overall deformation during the experiments is quasi-hydrostatic, individual powder particles experience a very heterogeneous deformation because of point contacts between the particles. Inspection of Fig. 4 reveals two obvious yield (kink bending) points for micron-Ni at $P_{\rm y1}$ = 0.4 GPa and $P_{\rm y2}$ = 1.6 GPa and the corresponding normalized strains at $\varepsilon_1^{\rm norm} = 0.7$ and $\varepsilon_2^{\rm norm} = 1.0$, respectively. The first yield represents micro/local grain-to-grain interactions that deform plastically because of high stress concentration during powder compaction. The second yield represents the macro/bulk plastic deformation of the entire sample, which is the true meaning of yield in classical mechanics.

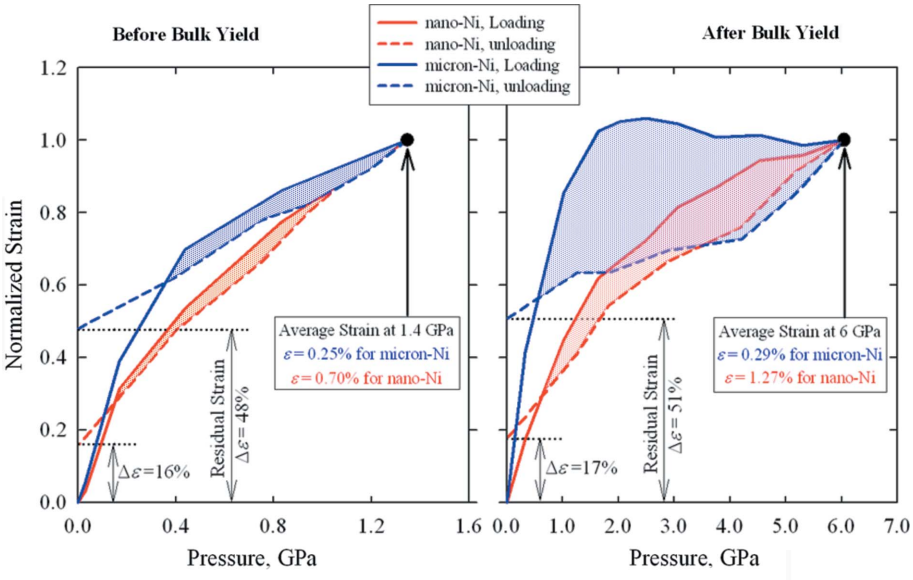

Figure 4
The normalized applied strain $\bar{\varepsilon}_{hkl}^{\rm ap} = (\Delta d/d)_{hkl}/(\Delta d/d)_{hkl}^{\max P}$, plotted as a function of pressure for nano-Ni (red lines) and micron-Ni (blue lines) during loading (solid lines) and unloading (dashed lines). For both panels, the plotted lines represent the averaged strains $\bar{\varepsilon}$ derived from four different lattice planes, (111), (200), (220) and (311). The average strains at the highest pressures, $P_{\rm max}$, are listed in the inserts.

The two-stage yield phenomenon is not as obvious in nano-Ni because it exhibits pronounced nonlinear ductility. Local plastic deformation is expected to take place at pressures much lower than 0.4 GPa, which is difficult to determine with our experimental techniques. On the other hand, work hardening to higher strain is clearly observed for nano-Ni. Nano-Ni also recovers a much larger fraction of the incurred strain upon unloading, 83–84% depending on maximum pressure, whereas micron-Ni only recovers 49–52%. The occurrence of unrecoverable strain can be caused by intergranular (*e.g.* elastic and plastic anisotropy) and/or intragranular (*e.g.* heterogeneous stress distribution and dislocation density) mechanisms. Previous studies (Budrovic *et al.*, 2004) have shown that nano-Ni shows full recovery of dislocation density when loaded in uniaxial tension. Interestingly, we observe that the recoverability for the nickel samples remains at about the same level for the unloading before and/or after the bulk yield. This, and the combination of almost full recovery for nano-Ni and less recovery for micron-Ni in our triaxial stress experiments, suggests that the unrecoverability of the plastic strain in nano-Ni is due to intergranular strain (elastic and plastic anisotropy), but it is mainly intragranular strain (dislocation density) in the micron-Ni.

The loading–unloading hysteresis loop illustrated in Fig. 4 is more significant for the after-yield samples (right-hand panel) than the before-yield samples (left-hand panel), despite comparable recoverability for both samples. Similar strain recoverability before and after yield indicates that the dislocation densities in the nickel samples become saturated in the elastic loading stage and that there is no further development in the plastic or ductile flow stage. The much larger hysteresis loop for micron-Ni after yield suggests that the high-P work on micron-Ni is dissipated as heat, as we have often experienced in the fatigue failure of nail bending. The dissipation loop is much smaller for the nano-Ni sample, indicating significantly reduced energy loss in its work-hardening plasticity deformation stage. The reduced level of energy dissipation for nano-Ni during the loading–unloading cycle indicates that nanostructured materials more readily endure greater mechanical fatigue in cyclic load-path changes. This is a significant discovery of nanomechanics.

3. Severe strains in nanocrystals and DER^2 corrections

We present a correction routine using diffraction elastic ratios (DERs) so that the significant data scatter in nanocrystalline materials can be reduced in a physically meaningful way. To reach the nanoscale, we must take into account the peak broadening

contribution from the crystal size. The Scherrer (1918) formula describes grain size in diffraction as

$$L = k\lambda/\Delta(2\theta)_{\rm size}\cos\theta, \tag{6}$$

where k is the Scherrer constant and $\Delta(2\theta)_{\rm size}$ is the FWHM in 2θ at a constant wavelength λ, in angular dispersive mode. By differentiating Bragg's diffraction equation, $\lambda = 2d\sin\theta$, with respect to d and 2θ, respectively, it becomes $\Delta(2\theta) = -2(\Delta d/d)\tan\theta$. We thus rewrite the Scherrer formula in terms of the d spacing,

$$L = kd^2/\Delta d_{\rm size}, \tag{7}$$

which is independent of the detection mode. We substitute $\Delta d_{\rm size} = kd^2/L$ into the Gaussian expression for the deconvoluted peak width and normalize the formula to a general definition of overall strain $\Delta d/d$, thus giving

$$\Delta d^2_{\rm obs}/d^2 = \left(\varepsilon^2 + \Delta d^2_{\rm ins}/d^2\right) + (k/L)^2 d^2(P, T). \tag{8}$$

The ordinate intercept of the $\Delta d^2_{\rm obs}/d^2$ *versus* $d^2(P, T)$ plot for a number of *hkl* diffraction indices presents the observed strain $\varepsilon^2_{\rm apparent} = \left(\varepsilon^2 + \Delta d^2_{\rm ins}/d^2\right)$, which includes the applied strain as well as the instrument contribution (*i.e.* the intrinsic peak width caused by instrument characteristics). It normalizes the peak-width span (lattice deformation) $\Delta d^2_{\rm obs}$ with respect to d^2, and the uncertainties associated with instrument calibrations, residual stresses and initial grain sizes are practically minimized. The grain size, L, is inversely proportional to the peak width and it can be derived from the slope $(k/L)^2$ of the $\Delta d^2_{\rm obs}/d^2$ *versus* $d^2(P, T)$ plot. We have demonstrated that the peak-width approach works well to derive high-P induced microstrain and particle-size reduction (grain crushing under loading) for hard and brittle ceramics and minerals in our recent high-P–T synchrotron X-ray diffraction studies (Zhang *et al.*, 2002; Chen *et al.*, 2005; Qian *et al.*, 2005).

Equation (8) can also be rewritten as $\left(\Delta d^2_{\rm obs} - \Delta d^2_{\rm ins}\right)/d^2 = \varepsilon^2 + (k/L)^2 d^2$, which seems to make sense in deriving applied strain and grain size under the given P–T conditions. However, one needs further to consider the illustration of residual stresses in comparative studies for the sample pair under ambient conditions (initial state, as well as the recovered state) and also to make straightforward graphical distinctions between the different parts of the contributions (instrument, grain size, and residual or recovered strains) to the observed peak-width changes. We recommend keeping equation (8) as a graphical deconvolution of diffraction profiles to better derive the thermomechanics of the sample materials.

We also performed a comparative high-P–T X-ray diffraction experiment on nano-Ni and micron-Ni. The high-pressure cell used is the same as that described in §2, except that amorphous carbon was used as the resistance heating material surrounding the boron nitride sample container. Plotted in Fig. 5 are normalized peak widths (or the observed strains) $\Delta d^2_{\rm obs}/d^2$ against $d^2(P, T)$ for nano-Ni at selected pressures and temperatures. Noticeably, the observed raw data (open black circles) scatter significantly, and this scatter is augmented as the pressure increases. Such large data scatter is not observed in our micron-Ni sample or other micrometre-scale-based experiments on ceramics and minerals. The increase in pressure also makes the micron-Ni data scatter gradually, although not to the level of the nano-Ni. We determine apparent variations in lattice strains according to different (*hkl*) diffraction planes and one cannot draw a simple straight line through the raw data to derive the microstrain and grain size from the plot. The fact that the (111) planes are not strained as much as the (200) planes reflects the lower elastic compliance of (111) when comparing the details of the lattice deformation.

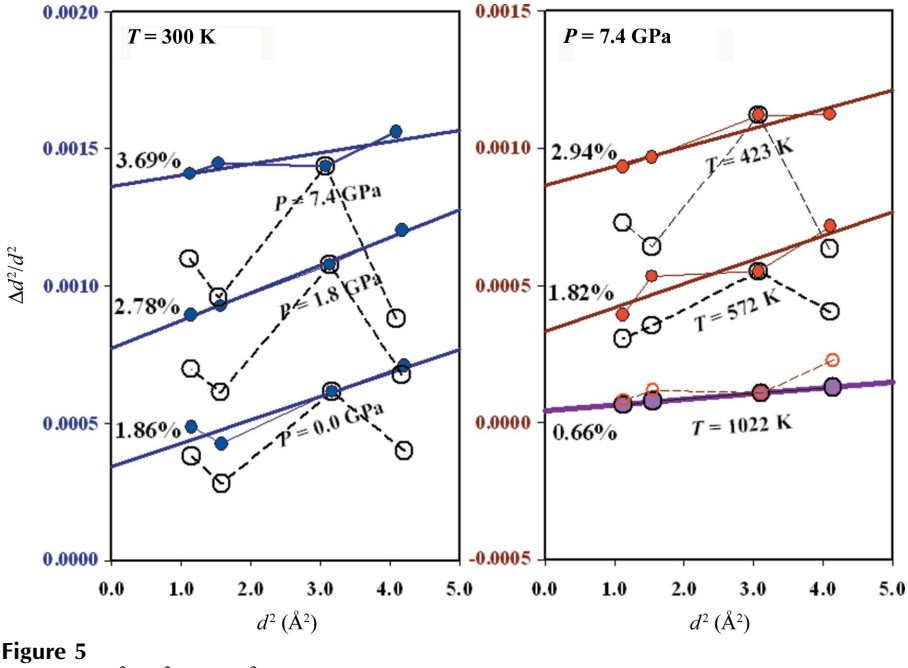

Figure 5
A plot of $\Delta d^2_{\rm obs}/d^2$ *versus* $d^2(P, T)$ for nano-Ni, according to equation (8). In both panels, the highly scattered raw data are shown as open black circles. The data corrected by $\rm DER^2 = (E_{hkl}/E_{200})^2$ are shown as solid blue symbols for the room-temperature data (left-hand panel) and as solid red symbols for the high-T data (right-hand panel). The straight lines show the linear regression results of the $\rm DER^2$ corrected data, with the ordinate intercepts providing apparent strains and the plot slopes providing gain-size information. The errors in the uncorrected $\Delta d^2_{\rm obs}/d^2$ are smaller than or comparable to the size of the plotted symbols.

Hooke's law relates the stress and strain tensors by $\varepsilon_{ij} = s_{ijmn}\sigma_{mn}$, where s_{ijmn} is the elastic compliance tensor. The stress components in our high-pressure experiments are close to quasi-isotropic, *i.e.* $\varepsilon = [(1 - 2\nu)/E]\sigma$, where ν is Poisson's ratio and E is Young's modulus. The diffraction elastic compliances S_1 and S_2 of the individual (*hkl*) planes for nickel metal are derived using single-crystal elastic constants for nickel (Simmons & Wang, 1971) and the mean field approach of Gnäupel-

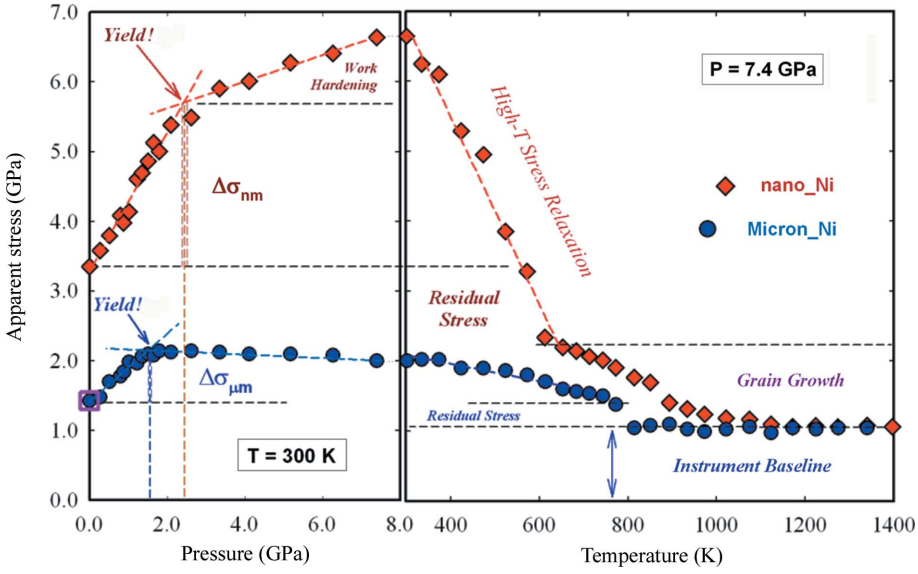

Figure 6
Apparent stresses for nano-Ni and micron-Ni, plotted as functions of pressure and temperature. The yield points are derived by the intersections of the elastic loading and plastic work-hardening or -softening stages. The corresponding high-P yield stresses are the stress differences $\Delta\sigma$ between the initial and yield states. The residual stresses of the samples should be read from the instrument baseline to the initial stress states under ambient conditions. The purple open square symbol is used to mark the recovered samples, which come back completely to the initial state of micron-Ni in terms of stress, strain and grain sizes. The errors in the strain determinations range from 0.05×10^{-2} to 0.1×10^{-2}, corresponding to errors of 0.1–0.2 GPa for the calculated apparent stress, which are smaller than or comparable to the size of the plotted symbols.

Herold *et al.* (1998). We further derive Young's modulus,

$$E_{hkl} = 1/(S_1 + S_2/2), \tag{9}$$

for different lattice planes based on the elastic compliance data and then normalize them to an E_{hkl}/E_{200} ratio, obtaining $E_{111}/E_{200} = 1.331$, $E_{200}/E_{200} = 1.000$, $E_{220}/E_{200} = 1.229$ and $E_{311}/E_{200} = 1.132$. By multiplying the square of the diffraction elasticity ratio,

$$\mathrm{DER}^2 = (E_{hkl}/E_{200})^2, \tag{10}$$

by the observed raw data (in the Gaussian expression), we correct the strain differences on individual lattice planes. By choosing the most compliant planes as our reference, the (200) peaks, we effectively obtain the upper bound for the apparent strain. For comparison, we show below the corrected strains using the least compliant plane, (111), for $\mathrm{DER}^2 = (E_{hkl}/E_{111})^2$, which would provide the lower bounds for the apparent strains. The corrected data (solid blue circles) can be readily fitted to a straight line in the $\Delta d^2_{\rm obs}/d^2$ *versus* $d^2(P, T)$ plot and allow us to derive the apparent strain and grain-size information unambiguously (see Fig. 5). By applying the DER^2 correction, we effectively eliminate or minimize the possible effects of changes in diffraction elasticity associated with the nanoscale and with P–T effects on individual elastic moduli. Under ambient conditions, the derived apparent initial strain is 1.86% for nano-Ni and 0.71% for micron-Ni. At P = 7.4 GPa, the apparent strain for nano-Ni almost doubles to 3.69% because of the applied stress. The corresponding high-P strain for micron-Ni has an increase of ~50%. Such differences in strain development reflect the fact that the deformation at interactions at grain corners and edges is more severe in the grain compaction of a nano-powder under high pressure.

The large scatter in the observed strains (raw data) is due to the different *hkl* elastic compliances of the crystal lattice and also reflects the high surface energy of the nanoscale particles. Compared with the grain core, the surface strain, also referred to as grain-boundary strain, of the nanocrystal shell is in a tensile mode for nano-Ni, based on Palosz's 'core–shell' model for nanocrystalline grains with an expanded surface layer (Palosz *et al.*, 2002, 2004). The correction using the ratio of diffraction elastic constants is applicable to nano-Ni but not to micron-Ni, because the surface strain becomes severe as the surface-to-core volume ratio increases dramatically in a nanocrystal. Therefore, the magnitude of the elastic correction may be deemed a good indication of the corresponding surface strain of the nanocrystalline grains. We have also demonstrated that in a Couchy expression of diffraction, *i.e.* without the square in equation (1), a DER correction is sufficient to reduce the data scatter, *i.e.* without the square in equation (10). Plotted in the right-hand panel of Fig. 5 are three selected data sets observed on high-temperature heating at P = 7.4 GPa. It is clear that the degree of data scatter decreases as the temperature increases and eventually, at $T \geq$ 893 K, all the raw data line up quite nicely as the stress level again becomes very low and the Ni crystal grains grow with increasing temperature.

4. Graphical derivation of thermomechanics

Apparent strains have been derived for nano-Ni and micron-Ni samples under all experimental conditions. The strains are then converted to stresses through $\sigma = E\varepsilon$, using the Young's modulus of E = 180 GPa for nano-Ni and E = 200 GPa for micron-Ni. This difference is because of an observed 10% reduction in the elastic modulus derivation from our recent EOS study of nano-Ni (Zhang *et al.*, 2007). The pressure and temperature derivatives on the elastic modulus are still ignored, but this should not affect the observation for the overall trend. The apparent stresses are plotted as a function of pressure and temperature in Fig. 6 to show thermo-mechanics comparisons between nano-Ni and micron-Ni. The initial difference between nano-Ni and micron-Ni is due to residual stress, surface strain and grain-size effects. As the pressure increases, the grain-to-grain contact stresses enhance at a much greater rate in nano-Ni during the elastic-to-plastic

transition region, *i.e.* in the stage from micro/local to macro/bulk yield. As the entire sample starts to loose its strength to support differential or shear stress, it is subjected to macro/bulk yield, and plastic deformation and/or viscous flow begins. Correspondingly, the diffraction peak widths do not vary as much after the bulk yield, indicating that the dislocation density in the crystalline sample reaches a certain saturation.

The derived yield stress of high-P triaxial compression is $\Delta\sigma_{\rm yield}^{\rm nm} \simeq 2.35$ GPa for nano-Ni (the ultimate yield $\sigma_{\rm y}$ minus the initial $\sigma_{\rm o}$), which is about the same as the uniaxial tensile strength of 2.25 GPa determined by Budrovic *et al.* (2004). The corresponding bulk yield stress (compression) of micron-Ni is $\Delta\sigma_{\rm yield}^{\mu\rm m} \simeq 0.75$ GPa, about a factor of three smaller than for nano-Ni. These observations are consistent with the classical Hall–Petch law (Hall, 1951; Petch, 1953), which indicates a significant increase in material strength as grain size decreases to the nanometre scale. The onset pressure for bulk yield in micron-Ni at $P_{\rm yield}^{\mu\rm m} \simeq 1.6$ GPa is also smaller than that for nano-Ni at $P_{\rm yield}^{\rm nm} \simeq 2.4$ GPa (Fig. 6, left). In the plastic stage, continuous peak broadening indicates strain hardening, whereas peak sharpening indicates strain softening under certain high-P–T conditions. There is an evident work hardening for nano-Ni, where the sample can still sustain higher differential or shear stress after the yield, and another $\Delta\sigma_{\rm nm} \simeq 1.0$ GPa is further loaded as the pressure increases to P = 7.4 GPa. However, the micron-Ni sample experiences a minor work softening at higher pressure.

It is well known that nano-metals have much less work hardening than the corresponding micro-metals in uniaxial tensile loading. Budrovic *et al.* (2004) observed very limited strain hardening in nano-Ni because of the suppressed accumulation of dislocations after plastic yield. Our triaxial compression data show the opposite phenomenon, which may be because of pressure effects. It is unlikely to arise from the artifacts resulting from the plot of $\varepsilon_{\rm ap}$ *versus* P (rather than the conventional σ *versus* ε), because the work hardening and work softening were observed in a comparative sense for the nano-Ni and micron-Ni samples under identical stress conditions.

As the temperature increases, the stress variation in nano-Ni exhibits two bending points, one at 600 K and the other near 1000 K (Fig. 6, right), dividing the stress–temperature variation into three different stages. Based on the grain-size analysis, which will be discussed in a later part of this paper, the stress reduction at T = 300–600 K largely reflects the relaxation of both the applied (differential) stresses and the surface strains in the Ni nanocrystals, whereas at T = 600–1000 K it is predominantly controlled by the grain growth. At $T > 1000$ K, the determined apparent stress does not show variation with increasing temperature, *i.e.* it reaches a flat trough in stress–temperature space. At these temperatures, the samples are defined to be in a stress-free state. Therefore, the initial surface or residual strain for nano-Ni can be graphically determined, as illustrated in the right-hand panel of Fig. 6, as 1.25×10^{-2}, which is in excellent agreement with the surface strain derived from neutron diffraction data at atmospheric pressure (see later discussion). This indicates the total removal of surface or residual strain and annealing of applied stress of about $\Delta\sigma_{\rm res}^{\rm nm} \simeq 2.5$ GPa at high temperatures in the range $550 < T < 1150$ K. For micron-Ni, the relaxation of apparent stress is not as vigorous as in nano-Ni and a true stress-free state is reached at $T \geq 800$ K. Similarly, the residual stress exerted upon the starting micron-Ni crystals (*i.e.* under initial ambient conditions) can be graphically derived and is about $\Delta\sigma_{\rm res}^{\mu\rm m} \simeq 0.35$ GPa.

The high-temperature data in the final portion of the experiment at $T > 1100$ K show a complete merging of nano-Ni and micron-Ni in terms of stress or strain levels, reconfirming the true stress-free states defined in the preceding paragraph. Therefore, the corresponding apparent strain is due to the instrument resolution, *i.e.* $\varepsilon_{\rm ap}^2 = \Delta d_{\rm ins}^2/d^2$, and there are no effects of microstrain and grain size at this stage. Our graphical approach using equation (8) demonstrates that the instrument contribution to the Bragg peak broadening (in units of Δd and further in strain and stress) can only be quantified with the sample itself when a true stress-free state is obtained through high-temperature annealing of a polycrystalline material. The true instrument contribution is usually difficult to characterize, particularly in energy-dispersive diffraction, because of the complexities of diffraction optics and instrument calibration. On the other hand, the residual strain and crystal defects such as dislocations further complicate the deconvolution of diffraction profiles. Fig. 6 is a graphical deconvolution of all types of contribution to the apparent stress, and a complete high-T annealing to a true stress-free state provides the instrument baseline for thermomechanical characterization. The graphical derivation using equation (8) is important not only for a comprehensive understanding of constituent behaviors, but also for the correct application of the peak-profile analysis method.

5. High-T grain growth and the annealing of nanostrain

Nanocrystalline crystallites are generally viewed as consisting of two structurally distinct components (see, for example, Gleiter, 1989; Palosz *et al.*, 2002, 2004), namely a single-crystal grain core and a surface shell layer characterized by a significant fraction of atoms at the strained surface. The fact that the diffraction peaks of nanocrystalline Ni under ambient conditions are significantly broader than those of microcrystalline Ni reflects the effects of both surface strain and grain-size reduction. To characterize their behavior at elevated temperatures with no external stress, and to practice our methodology further, we studied nano-Ni with time-of-flight (TOF) neutron diffraction in the temperature range 318–1073 K at atmospheric pressure. The nano-Ni sample is the same as the one we used in the high-P–T synchrotron X-ray diffraction experiments, and the measurements were carried out at the High-Pressure Preferred Orientation (HIPPO) beamline (Wenk *et al.*, 2003) of the Manuel Lujan Jr Neutron Scattering Center, Los Alamos National Laboratory, USA. For these measurements, the Ni powders were loaded into a quarter-inch-diameter vanadium can and heated in a stepwise increase of temperature *in vacuo*. The acquisition time for

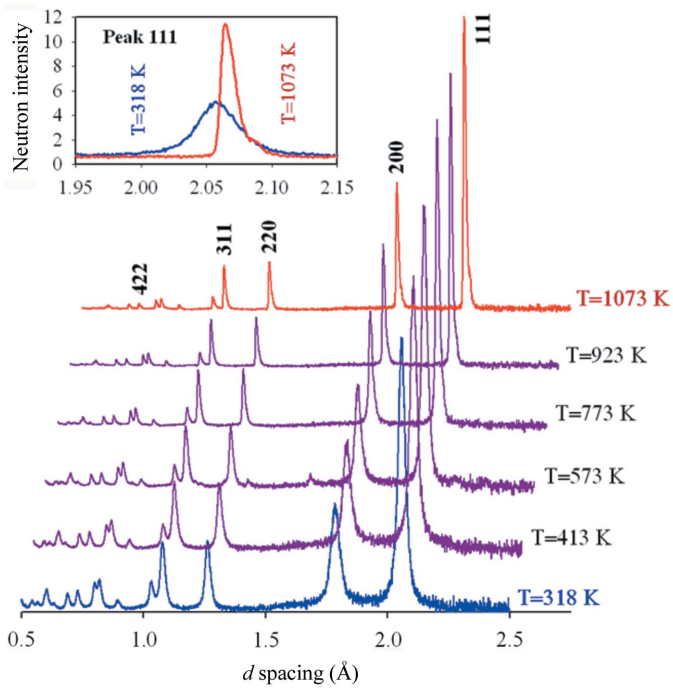

Figure 7
The time-of-flight neutron diffraction patterns for nano-Ni under atmospheric pressure and selected temperatures. The peak intensities of the *hkl* diffractions are normalized relative to that of (111) at T = 1073 K for width-comparison purposes. The insert shows an enlargement of a comparison of the (111) peak between T = 318 K and T = 1073 K, with the vertical axis being the measured neutron intensity.

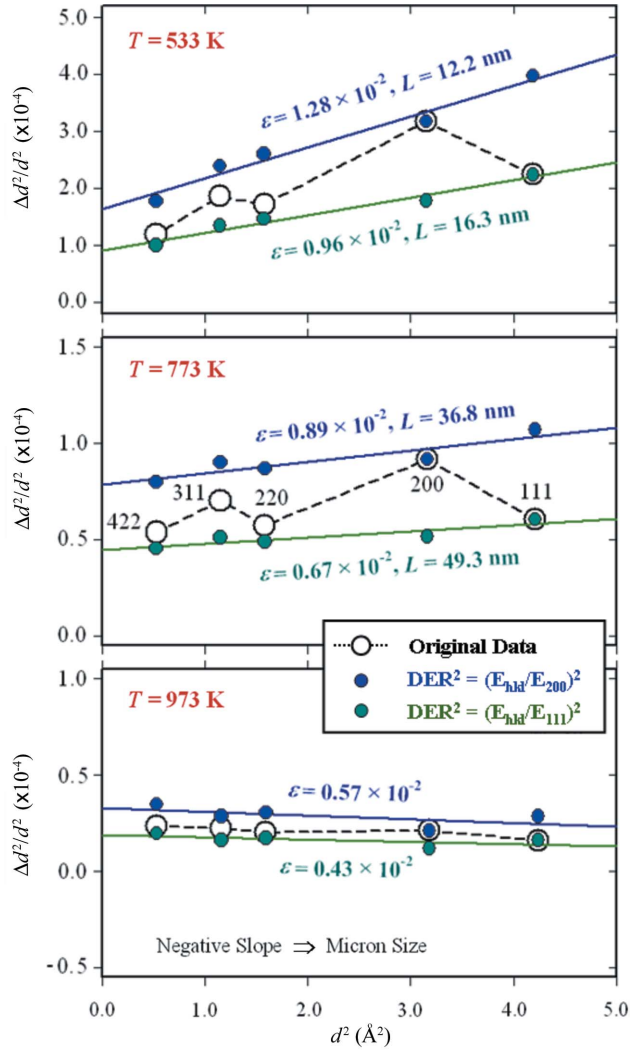

Figure 8
Plots of $\Delta d^2_{obs}/d^2$ *versus* $d^2(P, T)$ for neutron diffraction data on nano-Ni. The errors in the uncorrected $\Delta d^2_{obs}/d^2$ are smaller than or comparable to the size of the plotted symbols.

each diffraction pattern was 2 h. Plotted in Fig. 7 are the diffraction patterns at selected temperatures. Because of the large coverage of neutrons in Q space ($Q = 2\pi/d$), additional Bragg peaks at a small d spacing were observed compared with X-ray diffraction, of which the 422 peak can be used for strain derivation, therefore improving the peak-profile analysis for strain and grain size.

The peak positions (d) and FWHM (Δd) of the neutron diffraction data were determined by a single peak fitting of the diffracted intensity using the neutron TOF peak profile function No. 1 of the *General Structure Analysis System* (*GSAS*) package (Larson & Von Dreele, 2004). These data were then analyzed using equation (8), and the results at selected temperatures are plotted in Fig. 8. As observed in X-ray diffraction, Fig. 8 shows that the degree of data scatter decreases with increasing temperature and diminishes at temperatures above 873 K. In addition to the DER^2 correction with reference to soft E_{200}, we also applied the DER^2 correction relative to stiffer E_{111}, which would also provide lower bounds for strains and upper bounds for grain sizes. The E_{hkl}/E_{111} ratios applied (Simmons & Wang, 1971; Gnäupel-Herold *et al.*, 1998) are E_{111}/E_{111} = 1.000, E_{200}/E_{111} = 0.750, E_{220}/E_{111} = 0.923, E_{311}/E_{111} = 0.850 and E_{422}/E_{111} = 0.918. For both routines, the corrected data line up nicely in a linear fashion, which can be readily fit to equation (8) for the derivation of the surface strain (from ordinate interception) and grain size (from the slope of the regression line). Fig. 8 also reveals a peculiar behavior, in the sense that the slopes become negative for both the raw and the corrected data at $T \geq$ 873 K (see bottom panel) and grain-size information can no longer be extracted from equation (8). We consider this phenomenon as an indication of the growth of nanocrystals approaching or into the micrometre size region, therefore representing the limit of the present approach for grain-size analysis.

The grain sizes derived using equation (8) at all experimental temperatures are plotted in Fig. 9. The Ni nanocrystals do not show any growth at $T \leq$ 573 K, but they grow from 13.5 to 36.8 nm (with the E_{200} correction) or from 18.1 to 49.3 nm (with the E_{111} correction) in the temperature range 573–773 K. This growth process is accelerated at $T \geq$ 823 K, with the grain size quickly approaching or entering the micrometre region. Also plotted in Fig. 9 is the grain-size information derived from the high-temperature X-ray data at 7.4 GPa (*i.e.* the same diffraction data as used for the right-hand panel of Fig. 6). It is clear that the rate of grain growth at higher temperatures is considerably less at 7.4 GPa than at atmo-

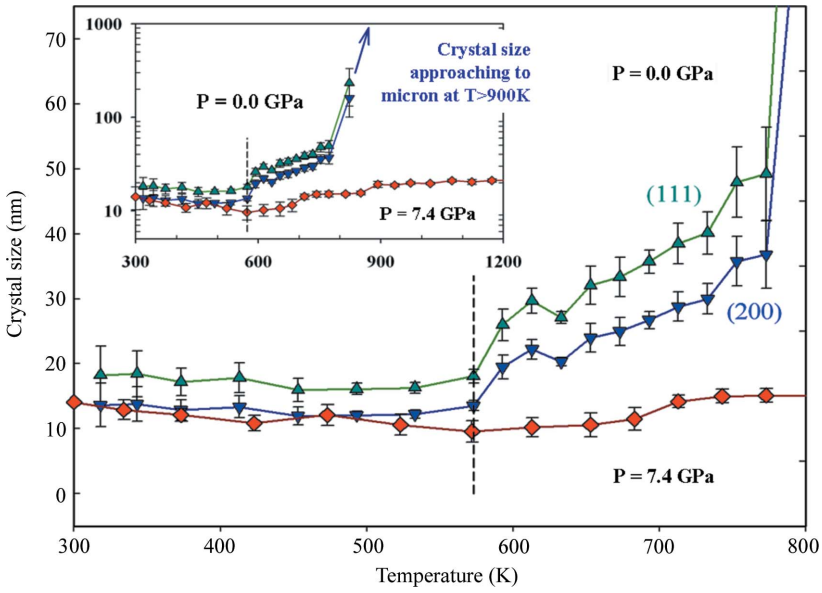

Figure 9
Variation of grain sizes for nano-Ni as a function of temperature at atmospheric pressure (neutron data) and at a high pressure of 7.4 GPa (X-ray data). For neutron data, the grain sizes derived from the $(E_{hkl}/E_{111})^2$ and $(E_{hkl}/E_{200})^2$ corrections are marked as (111) and (200), respectively, and are shown by solid green and blue triangles. Solid red diamonds denote the grain sizes derived from high-P–T X-ray data corresponding to Fig. 6. The insert plots the grain-size variation on a logarithmic scale and over a wider temperature range, showing the rapid growth of Ni nanocrystals approaching or entering the micrometre region.

spheric pressure. These observations indicate that pressure is an effective thermodynamic parameter that controls the crystallization process. Because the grain growth is typically accompanied by long-range atomic rearrangements, it would be kinetically hindered and/or suppressed at high pressures. The observations of Fig. 9 support our recent conclusion that pressure is a key controlling parameter for the synthesis of nanostructured ceramic materials (Zhao *et al.*, 2002, 2004).

Grain-size determination using equation (8) should be exercised with some caution. Powder diffraction peak profiles are usually not a pure Gaussian function, which is assumed in the present method. In the case of monochromatic diffraction, diffraction profiles depend on the mosaicity of the monochromator, beam collimation, beam divergence, energy half-width and aperture of the detector. In other words, they are significantly affected by instrumental contributions. Also, the conversion from scattering angle to d spacing would induce some distortion of the peak profiles. Taking into account all of these factors, the present method can be best applied to study variations of grain size with pressure and temperature, but it should be exercised with caution for the determination of the absolute value of grain size. Instrument effects on strain measurements should be less severe, owing to the relative nature of our graphical approach (subtraction), as illustrated in Fig. 6.

The apparent strains derived from neutron diffraction data are plotted as a function of temperature in Fig. 10. Clearly, the thermomechanical behavior of nano-Ni at atmospheric pressure shows the same trends as observed at 7.4 GPa (right-hand panel of Fig. 6), with two kinks (or two bending points) on the strain–temperature curves, one at 573 K and the other at 1023–1073 K. From Fig. 9, it is evident that the strain reduction in this high-temperature range is largely controlled by grain growth. Fig. 10 also reveals that a stress-free state is reached in Ni crystals at 1023–1073 K, making it graphically simple to quantify the instrumental baseline, which is $\varepsilon_{ins} = 0.4$–0.5×10^{-2} for the HIPPO neutron diffractometer, as obtained from the $(E_{hkl}/E_{111})^2$ and $(E_{hkl}/E_{200})^2$ corrected data. This graphical approach also makes it straightforward to determine the surface strain in nano-Ni by the subtraction of this baseline of instrument contribution. At $T = 318$ K, for example, the determined surface strain is 1.20–1.6 $\times 10^{-2}$, which is in good agreement with the residual strain of 1.25×10^{-2} derived graphically from the high-P–T nano-Ni data (Fig. 6).

6. Comparison with previous analytical techniques

A variety of diffraction peak-width analyses have been proposed to characterize the development of grain size and crystal strain, primarily based on the well known Scherrer formula and the WH method or its modifications (Gerward *et al.*, 1976; Westwood *et al.*, 1995; Weidner, 1998; Ungár & Tichy, 1999). In all these approaches, the peak breadths are typically

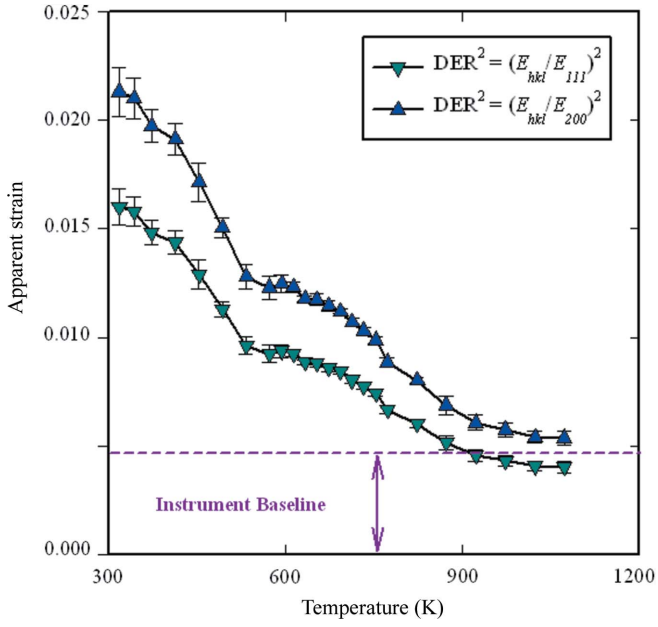

Figure 10
Variation of the apparent strains for nano-Ni as a function of temperature at atmospheric pressure (neutron diffraction). The plotted apparent strains include both the surface strains of the Ni nanocrystals and the instrument contribution. The plot also reveals similar thermomechanics behavior to that observed at high P–T (Fig. 6).

expressed in units of the Bragg diffraction angle or X-ray photon energy. Because all diffraction techniques, including energy dispersive (keV), angular dispersive (2θ) and time-of-flight (μs), observe the d spacing of various hkl lattice planes, we plot the diffraction peak profile on a length scale (Å) that is a universal expression of the peak breadth, and is thus independent of the detection mode, using the lattice d spacing. Our graphical deconvolution method, equation (8) and the $\Delta d^2_{obs}/d^2$ *versus* $d^2(P, T)$ plot, has a significant advantage over the previous methods of peak-profile analysis for strain and grain size. Also, because the instrument contribution to the diffraction peak profile is quite complex, as shown in this study, one cannot simply subtract it before the least-squares fits. We have learned from the current study that measurements on a reference material, either a standard material or the sample itself under ambient conditions, may not provide an accurate baseline for the instrumentation correction. The complex convolution of the diffraction profile may be misrepresented in these simple subtractions of peak broadening.

6.1. The classical Williamson–Hall approach

The WH approach is a popular method for the analysis of diffraction line broadening caused by strain and small crystal size. The general expression for this analysis is given as (Klug & Alexander, 1974; Warren, 1989)

$$\beta_o^2 - \beta_i^2 = \beta_L^2 + \beta_S^2, \tag{11}$$

where β_o^2 is the observed peak breath, β_i^2 is the instrumental contribution, β_L^2 is the grain size broadening and β_S^2 is the strain broadening. In angular-dispersive diffraction, $\beta_L = k/L$, and $\beta_S = 2\varepsilon K$, where k is the Scherrer constant, L the average crystal size, ε the average strain and $K = 2\sin\theta/\lambda$ (θ and λ are the Bragg angle and X-ray wavelength, respectively). For energy-dispersive diffraction (Gerward *et al.*, 1976), $\beta_L = k(hc/2)/(L\sin\theta)$ and $\beta_S = 2\varepsilon E$, where h is Planck's constant, c the velocity of light and E the X-ray photon energy. The instrumental broadening is typically measured using a microcrystalline material that is assumed to be strain-free. Once this component is subtracted from the observed profiles, a simple WH plot of $\beta_o^2 - \beta_i^2$ *versus* K^2 or E^2 for a number of different diffraction peaks would provide estimated values of L and ε from the intercept and slope, respectively.

As discussed in §1, the classical WH formulation can be rewritten using the universal length scale of the d spacing, as given by equation (3). To perform the WH analysis on nano-Ni data (Fig. 7), we also collected neutron diffraction patterns for micrometre-size (3–7 μm) polycrystalline Ni to obtain the instrumental broadening of the Bragg peaks. Using equation (3), along with our DER^2 correction routines, we analyzed the neutron diffraction data for nano-Ni, and selected results are shown in Fig. 11. As expected, the corrected data for both $E(111)$ and $E(200)$ line up nicely for linear regression. However, at all temperatures up to 823 K, the least-squares fits give rise to negative intercepts, making it impossible to determine the grain sizes. The problem, as discussed earlier, primarily comes from the instrumental contribution to the peak broadening, which is usually not easy to characterize in view of the complexity of polycrystalline materials; issues such as the existence of residual strain and line defects must be considered. On the other hand, our graphical approach (Figs. 6 and 10) does not need the comparative studies used in the sample-pair subtraction technique for the instrument correction. The high-T measurements eventually reach the true stress-free state, and the instrument baseline for strain (not peak width) can be subtracted in a straightforward manner.

6.2. Modified WH method – the Ungár approach

A limitation of the classical WH method is that strain anisotropy effects are not taken into account. For materials (particularly nanocrystalline materials) containing massive dislocations, WH plots usually present considerable scatters that are beyond the experimental uncertainties (see, for example, Shen *et al.*, 2005), as also demonstrated for nano-Ni

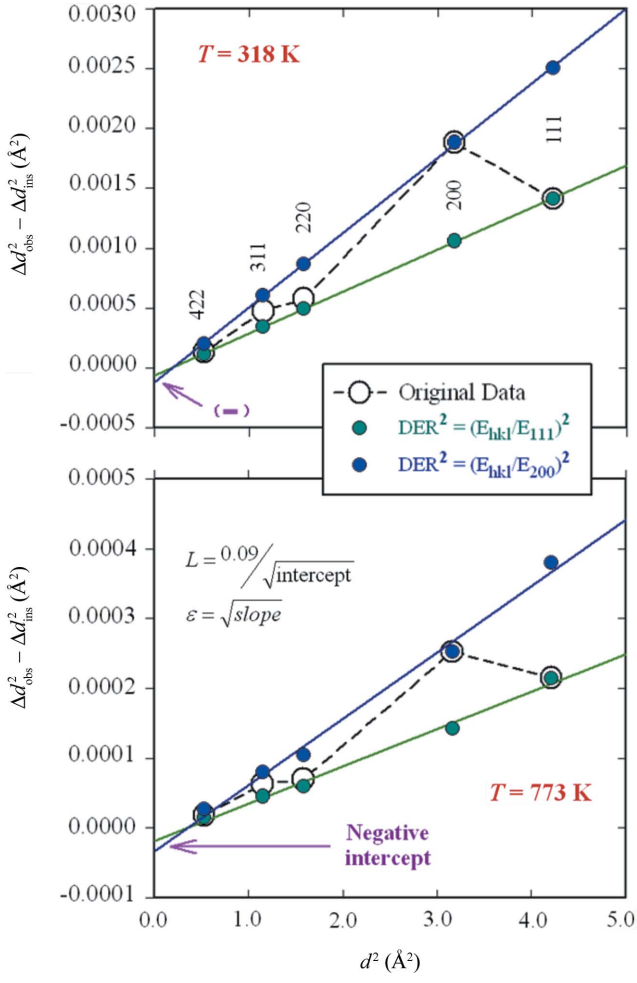

Figure 11
Classical Williamson–Hall plots using the length scale of the d spacing for the Bragg peak width. The data plotted here are from TOF neutron diffraction for nano-Ni at 318 K (upper panel) and 773 K (lower panel), which are derived from the same diffraction data as used for Figs. 8 and 9. The instrument contribution of Δd_{ins} is derived from the sample pair of micron-Ni data under ambient conditions. The errors in the uncorrected $\Delta d^2_{obs}/d^2$ are smaller than or comparable to the size of the plotted symbols.

in this work. In recent years, Ungár and coworkers proposed a modified WH formula to account for diffraction peak broadening as a result of line defects (Révész *et al.*, 1996; Ungár & Tichy, 1999; Ungár *et al.*, 1999). In this approach, dislocations are assumed to be the main contributors to the residual strain and, correspondingly, the scatter in the WH plot is attributed to the anisotropy of the dislocation strain field. In the Ungár approach, the modified WH formula is given by

$$(\Delta K)^2 = \left(\frac{0.9}{L}\right)^2 + \left(\frac{\pi b^2 \rho}{2A}\right) K^2 C, \qquad (12)$$

where $\Delta K = \beta_o - \beta_i$, b is the modulus of the Burgers vector of dislocations, ρ is the dislocation density, A is a constant [~10 for a wide range of dislocation distribution; see Ungár *et al.* (1999)] and C is the contrast factor of dislocations for Bragg reflection hkl. The value of C_{hkl} can be calculated from the contrast factor for Bragg reflection (h00), according to

$$C_{hkl} = C_{h00}(1 - qH^2), \qquad (13)$$

where $H^2 = (h^2k^2 + h^2l^2 + k^2l^2)/(h^2 + k^2 + l^2)^2$ for a cubic crystal system, and q is a constant deduced from a forced fit to the data. For cubic materials, the contrast factor C depends on the elastic anisotropy S [$= 2C_{44}/(C_{11} - C_{12})$] and the ratio C_{12}/C_{44}, where C_{11}, C_{12} and C_{44} are the elastic constants (Révész *et al.*, 1996). More detailed procedures for data analysis using equation (12) were presented in the work of Shen *et al.* (2005).

Because $K = 2\sin\theta/\lambda = 1/d$, one can also rewrite equation (12) using the universal length scale of the d spacing, giving (Shen *et al.*, 2007)

$$\left(\frac{\Delta d}{d^2}\right)^2 = \left(\frac{0.9}{L}\right)^2 + \left(\frac{\pi b^2 \rho}{2A}\right)\left(\frac{C}{d^2}\right), \qquad (14)$$

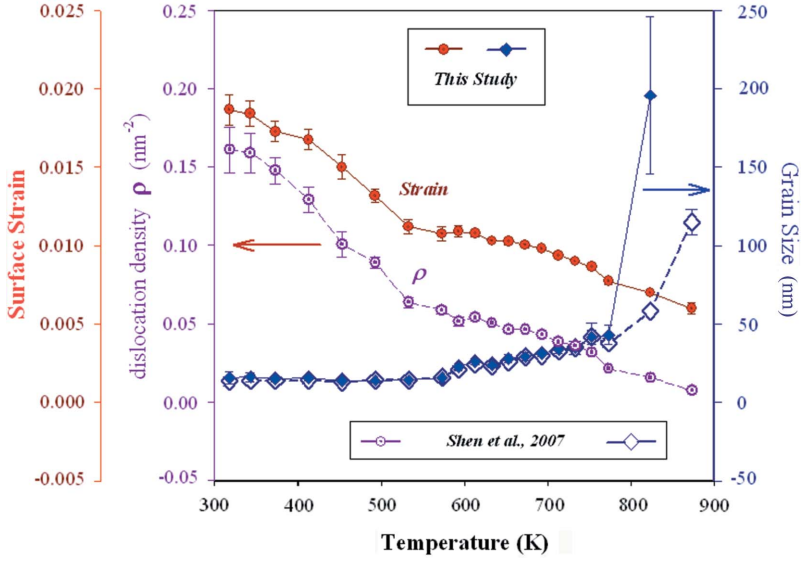

Figure 12
High-T annealing and grain growth of nanocrystalline nickel. Comparison of the results of the peak-profile analysis between our approach (equation 8; this study) and the Ungár approach (equation 14; Shen *et al.*, 2007).

where Δd is the FWHM of the neutron diffraction peaks with the instrumental broadening already subtracted. Shen *et al.* (2007) applied equation (14) to derive the dislocation density and grain size for all high-temperature neutron data on nano-Ni, and their results are reproduced in Fig. 12. For comparison with our approach [equation (8)], we take the average values of the two DER[2] correction routines for grain size and strain (Figs. 9 and 10) and also plot them in Fig. 12. It is evident that the two methods give rise to comparable results for grain-size analysis, in both absolute values and their variation with temperature. The dislocation densities derived from the Ungár method also show the same trends of variation with temperature as the surface strains we derived from equation (8). Specifically, there is a bending point near 573 K where the rate of reduction in dislocation density or surface strain coincides with grain growth in Ni nanocrystals. Following Ashby (1970) and Ashby & Jones (1986), dislocations in plastically deformed crystals can be separated into 'geometrically necessary' dislocations (those associated with the existence of grain boundaries) and 'statistically stored' dislocations (glissile dislocations participating in the plastic deformation). In Ni nanocrystals, these two different types of dislocations are found to correlate with the grain-size variation, as discussed in detail by Shen *et al.* (2007). Note that in the Ungár method the dislocation density is a parameter that characterizes the surface or residual strains caused by crystalline dislocations. Therefore, although it is not parametrically equivalent to the surface strain we determined, both of them describe similar physical performance of nanocrystals. Also, the dislocation density of the Ungár approach and the surface or residual strain of our study show similar trends of variation. As high-T annealing becomes more effective at $T > 900$ K, the surface strain approaches the instrument baseline of $\varepsilon_{ins} = 0.005$ for our derivation and the dislocation density approaches zero, because the Ungár approach has already subtracted the instrumental contribution to the peak broadening in advance. The minor deviation of the two approaches as the temperature changes may come from the two different elastic corrections employed in the DER[2] correction routine (this study) and in C_{hkl} (Ungár's approach).

It is worthwhile to mention that recent developments using submicrometre X-ray beams (Yang *et al.*, 2004; Ice *et al.*, 2005; Levine *et al.*, 2006) make it possible to predict the evolution of dislocation distributions and the resulting local stresses. These measurements provide a critical means for validating and guiding the development of detailed dislocation-based simulations and models. We expect such quantitative and spatially resolved measurements down to dislocation-cell level to be of particular relevance to microstructural studies using the Ungár approach for the analysis of diffraction line profiles.

7. Conclusion

Starting from a general definition of overall strain $\Delta d/d$ in the Gaussian expression for diffraction peak profiles, and also on the basis of the Williamson–Hall method and the Scherrer formula, we have developed an analytical method to derive the thermomechanical properties of loading stress, yield stress, work hardening, work softening and thermal relaxation under high-pressure and/or high-temperature conditions. This method deals with non-uniform stress among heterogeneous crystal grains, as well as surface strain in nanocrystalline materials, by examining the peak-width variation under different P–T conditions. Because the method is based directly on the lattice d spacing and the local stress-induced lattice deformation Δd, it can be applied to any diffraction profile, independent of the detection mode. We have also developed a correction routine, DER^2, using diffraction elastic ratios to process the severe surface or residual strain data and/or strain anisotropy effects related to nano-scale grain sizes, so that the significant data scatter can be reduced in a physically meaningful way. The graphical derivation of microstrain under high-P–T conditions allows the instrumental contribution to be illustrated and subtracted in a straightforward manner, thus avoiding the potential complexities and errors caused by the instrument correction.

Yield strength (σ_y) is an important constitutive property of materials to define the onset of plastic deformation and viscous flow. The yield strengths of crystalline materials as a function of pressure and temperature have been documented previously, although infrequently. Through case studies of hard ceramic materials (6H-SiC) and soft metals (nano-Ni and micron-Ni) using energy-dispersive X-ray and time-of-flight neutron diffraction, our analytical method can clearly identify micro/local yield at grain-to-grain contacts resulting from high stress concentration, and macro/bulk yield for plastic deformation over an entire sample. This simple and straightforward graphical approach for microstrain analysis can also reveal the corresponding yield stress, grain crushing and grain growth, work hardening and work softening, and thermal relaxation under high-P–T conditions, as well as the intrinsic residual or surface strain in the polycrystalline bulk. We strongly recommend that a thorough deformation study of plasticity should include high-temperature annealing to reach a true stress-free state. This is important not only for a comprehensive understanding of thermomechanical behavior but also for the correct application of the peak-profile analysis method.

We are grateful to two anonymous referees for pointing out the errors in correlating FWHM and s in equation (1), and for other comments that helped to improve the manuscript. This research was supported by Los Alamos National Laboratory, which is operated by Los Alamos National Security LLC under the Department of Energy, contract No. DE-AC52-06NA25396. The high-temperature neutron experiments were performed on the HIPPO beamline of the Lujan Neutron Scattering Center at LANSCE, which is funded by the Department of Energy's Office of Basic Energy Sciences. The high-P–T X-ray diffraction experiments were carried out on the X17B2 beamline of the National Synchrotron Light Source, Brookhaven National Laboratory, which is supported by the Consortium for Materials Properties Research in Earth Sciences (COMPRES) under the National Science Foundation Cooperative Agreement EAR 01-35554.

References

Ashby, M. F. (1970). *Philos. Mag.* **21**, 399–424.
Ashby, M. F. & Jones, D. R. (1986). *Engineering Materials 2: An Introduction to Microstructures, Processing and Design*, p. 369. Oxford: Pergamon Press.
Brown, D. W., Bourke, M. A. M., Clausen, B., Holden, T. M., Tome, C. N. & Varma, R. A. (2003). *Metall. Mater. Trans. A*, **34**, 1439–1449.
Budrovic, Z., Van Swygenhoven, H., Derlet, P. M., Van Petegem, S. & Schmitt, B. (2004). *Science*, **304**, 273–276.
Chen, J., Schmidt, N., Chen, J. H., Zhang, J., Wang, L. & Weidner, D. J. (2005). *J. Mater. Sci.* **40**, 5763–5766.
Decker, D. L. (1971). *J. Appl. Phys.* **42**, 3239–3244.
Feng, R., Raiser, G. F. & Gupta, Y. M. (1996). *J. Appl. Phys.* **79**, 1378–1387.
Feng, R., Raiser, G. F. & Gupta, Y. M. (1998). *J. Appl. Phys.* **83**, 79–86.
Gerward, L., Morup, S. & Topsoe, H. (1976). *J. Appl. Phys.* **47**, 822–825.
Gleiter, H. (1989). *Prog. Mater. Sci.* **33**, 223–315.
Gnäupel-Herold, T., Brand, P. C. & Prask, H. J. (1998). *J. Appl. Cryst.* **31**, 929–935.
Hall, E. O. (1951). *Proc. Phys. Soc. London Sect. B*, **64**, 747–753.
Ice, G. E., Larson, B. C., Tischler, J. Z., Liu, W. & Yang, W. (2005). *Mater. Sci. Eng. A*, **399**, 43–48.
Klug, H. P. & Alexander, L. E. (1974). Editors. *X-ray Diffraction Procedures for Polycrystalline and Amorphous Materials*, 2nd ed. New York: Wiley.
Larson, A. C. & Von Dreele, R. B. (2004). *GSAS*. Report LAUR 86-748. Los Alamos National Laboratory, New Mexico, USA.
Levine, L. E., Larson, B. C., Yang, W., Kassner, M. E., Tischler, J. Z., Delos-Reyes, M. A., Fields, R. J. & Liu, W. J. (2006). *Nat. Mater.* **5**, 619–622.
Palosz, B., Grzanka, E., Gierlotka, S., Stel'makh, S., Pielaszek, R., Bismayer, U., Neuefeind, J., Weber, H. P., Proffen, T., Von Dreele, R. & Palosz, W. (2002). *Z. Kristallogr.* **217**, 497–509.
Palosz, B., Stel'makh, S., Grzanka, E., Gierlotka, S., Pielaszek, R., Bismayer, U., Werner, S. & Palosz, W. (2004). *J. Phys. Condens. Matter* **16**, S353–S377.
Petch, N. J. (1953). *J. Iron Steel Inst.* **174**, 25–28.
Qian, J., Pantea, P., Zhang, J., Zhao, Y., Wang, Y. & Uchida, T. (2005). *J. Am. Ceram. Soc.* **88**, 903–906.
Révész, Á., Ungár, T., Borbély, A. & Lendvai, J. (1996). *Nanostruct. Mater.* **7**, 779–788.
Scherrer, P. (1918). *Nachr. Ges. Wiss. Göttingen Math. Phys. Kl.* **26**, 98–100.
Shen, T. D., Schwarz, R. B., Feng, S. H., Swadener, J. G., Huang, J. Y., Tang, M., Zhang, J. Z., Vogel, S. C. & Zhao, Y. S. (2007). *Acta Mater.* **55**, 5007–5013.
Shen, T. D., Schwarz, R. B. & Thompson, J. D. (2005). *Phys. Rev. B*, **72**, 014431.
Simmons, G. & Wang, H. (1971). *Single Crystal Elastic Constants.* Cambridge: MIT Press.
Ungár, T., Dragomir, I., Révész, Á. & Borbély, A. (1999). *J. Appl. Cryst.* **32**, 992–1002.
Ungár, T. & Tichy, G. (1999). *Phys. Status Solidi A*, **171**, 425–434.
Vaughan, M. T, Weidner, D. J., Wang, Y., Chen, J., Koleda, C. C. & Getting, I. C. (1998). *Rev. High Press. Sci. Technol.* **7**, 1520–1522.
Wang, Y., Zhang, J. & Zhao, Y. (2007). *Nano Lett.* **7**, 3196–3199.
Warren, B. (1989). *X-ray Diffraction*. London: Addison-Wesley.

Weidner, D. J. (1998). *Ultrahigh-Pressure Mineralogy: Physics and Chemistry of the Earth's Deep Interior*, edited by R. J. Hemley & H. K. Mao, pp. 493–524. Washington, DC: Mineralogical Society of America.
Weidner, D. J., Vaughan, M. T., Ko, J., Wang, Y., Liu, X., Yeganeh-Haeri, A., Pacalo, R. E. & Zhao, Y. (1992). *High-Pressure Research: Application to Earth and Planetary Sciences*, edited by Y. Syono & M. H. Manghnani, Geophysics Monograph Series, Vol. 67, pp. 13–17. Washington, DC: American Geophysical Union.
Weidner, D. J., Wang, Y. & Vaughan, M. T. (1994). *Science*, **266**, 419–422.
Wenk, H. R., Lutterotti, L. & Vogel, S. (2003). *Nucl. Instrum. Methods Phys. Res. Sect. A*, **515**, 575–588.
Westwood, A. D., Murray, C. E. & Noyan, I. C. (1995). *Advances in X-ray Analysis*, edited by P. K. Predecki, T. C. Huang, D. K. Bowen, J. V. Gilfrich, I. C. Noyan, C. C. Goldsmith, R. Jenkins & D. K. Smith, Vol. 38, pp. 243–254. Heidelberg: Springer.
Williamson, G. K. & Hall, W. H. (1953). *Acta Metall.* **1**, 22–31.
Yang, W., Larson, B. C., Tischler, J. Z., Ice, G. E., Budai, J. D. & Liu, W. (2004). *Micron*, **35**, 431–439.
Zhang, J., Wang, L., Weidner, D. J., Ucchida, T. & Xu, J. (2002). *Am. Mineral.* **87**, 1005–1008.
Zhang, J., Zhao, Y. & Palosz, B. (2007). *Appl. Phys. Lett.* **90**, 043112.
Zhao, Y., He, D., Daemen, L. L., Huang, J., Shen, T. D., Schwarz, R. B., Zhu, Y., Bish, D. L., Zhang, J., Shen, G., Liu, Z., Qian, J. & Zerda, T. W. (2002). *J. Mater. Res.* **17**, 3139–3145.
Zhao, Y., Qian, J., Daemen, L. L., Pantea, C., Zhang, J., Voronin, G. & Zerda, T. W. (2004). *Appl. Phys. Lett.* **84**, 1356–1368.
Zhao, Y., Weidner, D. J., Ko, J., Leinenweber, K., Liu, X., Li, B., Meng, Y., Pacalo, R. E. G., Vaughan, M. T., Wang, Y. & Yeganeh-Haeri, A. (1994). *J. Geophys. Res.* **99**, 2871–2885.
Zhao, Y. & Zhang, J. (2007). *Appl. Phys. Lett.* **91**, 201907.
Zhao, Y., Zhang, J., Clausen, B., Shen, T. D., Gray, G. T. III & Wang, L. (2007). *Nano Lett.* **7**, 426–432.